Supporting Information

Deep ion mass transfer addressing the capacity shrink challenge of aqueous Zn||MnO$_2$ batteries during the cathode scaleup

Na Jiang[1#], You Zeng[1#], Qi Yang*[1], Puda Lu[1], Keqi Qu[1], Lihang Ye[1], Xuejun Lu*[1], Ziqiang Liu[1], Xixian Li[1], Yongchao Tang[3], Jinchao Cao[5], Shimou Chen[4], Chunyi Zhi[2], Jieshan Qiu*[1]

[1] State Key Laboratory of Chemical Resource Engineering, College of Chemical Engineering, Beijing University of Chemical Technology, Beijing 100029, China

[2] Department of Materials Science and Engineering, City University of Hong Kong, 83 Tat Chee Avenue, Kowloon, Hong Kong 999077, China

[3] School of Chemical Engineering and Light Industry, Guangdong University of Technology, Guangzhou 510006, China

[4] State Key Laboratory of Chemical Resource Engineering College of Materials Science and Engineering, Beijing University of Chemical Technology, Beijing 100029, China

[5] Binzhou Institute of Technology, Weiqiao-UCAS Science and Technology Park, Binzhou 256600, China

[#] These authors contribute equally to this work.

E-mail: qi.yang@mail.buct.edu.cn; xj.lu@buct.edu.cn; qiujs@mail.buct.edu.cn

Experimental Section

Material preparation. Pitch (1 g, Shenhua, China) and manganese chloride tetrahydrate ($MnCl_2 \cdot 4H_2O$) (3 g, Aldrich) were dissolved into anhydrous ethanol (20 mL) via stirring for 12 hours, followed by drying in an oven at 60 °C until the ethanol was completely evaporated. The product was then ground into powder. The powder was loaded on the corundum boat and placed in a tube furnace under a nitrogen atmosphere and then heated to 800 °C at a ramping rate of 5 °C min^{-1}, followed by maintaining at 800 °C for 2 hours to obtain a compound of carbon and manganese oxide. Afterwards, the mixture is mixed with $NaHCO_3$ (molar ratio 1:1) at room temperature for 1 h, and filtered, then dried in vacuum oven at 60 °C. During the next oxidation process, the compound was placed in a Muffle furnace under an air atmosphere and heated to 300 °C at a ramping rate of 5 °C min^{-1}. After the treatment at 300 °C for 2, 4, 6, and 8 h, IC@MnO_2 was obtained. The bare γ-phase MnO_2 was purchased (Xiangtan Weixin manganese products Co., LTD).

Characterization Methods. Powder XRD patterns were collected on an X-ray diffractometer (Bruker D8 Advance, Germany) with Cu Kα radiation ($\lambda = 0.15406$ nm) at 40 Kv, 30 mA. SEM images and EDX mapping were obtained on a Field-emission TESCAN MIRA LMS microscope with equipped energy dispersive spectroscopy. TEM and HRTEM images were collected by a JEOL JEM-F200 microscope instrument with the equipped EDS. XPS was tested on a Thermo Scientific K-Alpha equipped with a hemispherical analyzer. Raman spectra were obtained on LabRAM Aramis Raman Microscope using 532 nm excitation. TG was measured by a STA7300 (HTIACHI, Japan) analyzer with an airflow. Fourier transform infrared spectroscopy (FT-IR) spectrum was recorded with a TENSOR II FT-IR Spectrometer using KBr pellets. Mn K-edge XANES measurements were performed at the Institute of High Energy Physics, Chinese Academy of Sciences (Beijing, China). The content of zinc and manganese in the cathodes was measured using an ICP-OES 5800.

Electrochemical measurements. In a typical process, IC@MnO_2 or MnO_2 was mixed with Super P Carbon and polyvinylidene difluoride (PVDF) with a weight ratio of 7:2:1 to form a homogeneous slurry. Then, the slurry was cast onto a piece of carbon cloth and then dried in a vacuum oven at 60 °C for 12 hours. Electrochemical measurements were performed with CR2032 coin-type cell. Zinc plate with a thickness of 0.1 mm, glass fiber, and aqueous 2 M $ZnSO_4$ with 0.1 M $MnSO_4$ was used as the anode, separator, and electrolyte, respectively. The area size of the electrode is 1×1 cm^2, the amount of electrolyte in each coin-type cell is about 160 μL, and the loading masses of active materials are set as about 1, 5, and 10 mg cm^{-2}, respectively. Battery performance tests were conducted with LANHE battery testing systems for cycling stability. For battery with a large cathode loading mass, an activation procedure is conducted. Other electrochemical tests such as CV were measured by a CHI660E electrochemical workstation (Shanghai Chenhua Instrument Co., China).

Theoretical calculation. DFT based first-principles calculations are performed using the projected augmented wave (PAW) method implemented in the Vienna ab initio simulation package (VASP). The generalized gradient approximation (GGA) with Perdew Burke-Ernzerhof (PBE) functional and the projector augmented wave (PAW) potential were

employed. The kinetic energy cut-off was set to 450 eV. The Brillouin-zone (BZ) integration is carried out using the Monkhorst-Pack sampling method with a density of 3×2×1 for simulations. A sufficiently large vacuum region of 15 Å was used for all the systems to ensure the periodic images were well separated. The convergence criterion of force and energy were set to 0.02 eV Å^{-1} and 10^{-5} eV, respectively. The pathways of adsorption energy on the considered models were calculated in detail according to the electrochemical framework developed by Norskov et al.:

$$E_{ads} = E_{AB} - E_A - E_B \qquad (5)$$

GITT measurements

GITT measurements were used to test the diffusion coefficient of zinc ions (D_{Zn2+}) in the cathode based on the following equation:

$$D_{Zn^{2+}} = \frac{4}{4\pi}\left(\frac{mv}{MA}\right)^2\left(\frac{\Delta E_s}{\Delta E_t}\right)^2$$

where m (g) and M (g mol^{-1}) are assigned to the loading mass and molecular weight of active material; V (cm^3 mol^{-1}) represents the molar volume of materials deduced from crystallographic data; τ (s) is constant current pulse time; A (cm^2) is the surface area of electrode; ΔE_s (V) and ΔE_t (V) denote the change of steady-state voltage and the total change of the voltage during a constant pulse for a single-step GITT curve, respectively. A current density of 200 mA g^{-1} is applied to the ZIBs with τ= 2 min and then stood for 30 min without current impulse.
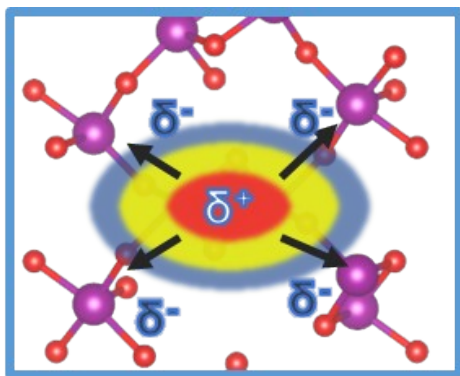
Figure S1. The schematic illustration of corresponding charge transfer behavior around the carbon site.
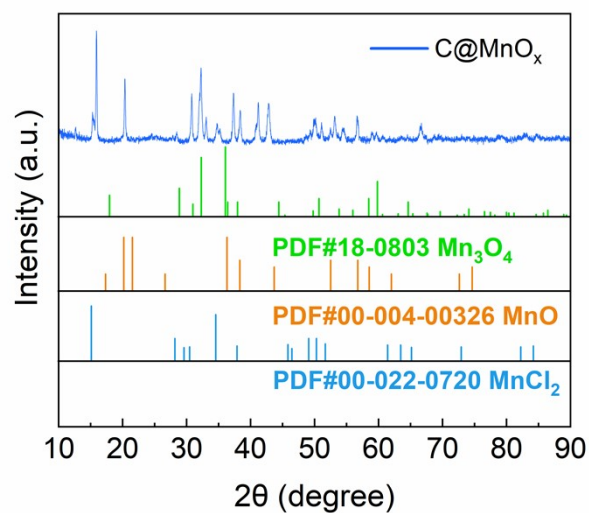
Figure S2. XRD pattern of the manganese oxides and carbon composite (C@MnO$_x$). This XRD data show that during the annealing in nitrogen, the MnCl$_2$ was gradually transformed to MnO and Mn$_3$O$_4$, where the oxygen comes from pitch.
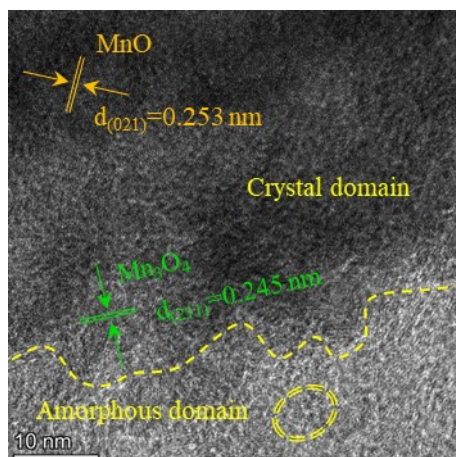
Figure S3. Transmission electron microscope (TEM) image of MnO$_x$@C. This result agrees well with the XRD data. We can find the phases of MnO and Mn$_3$O$_4$ beside the amorphous carbon domain.
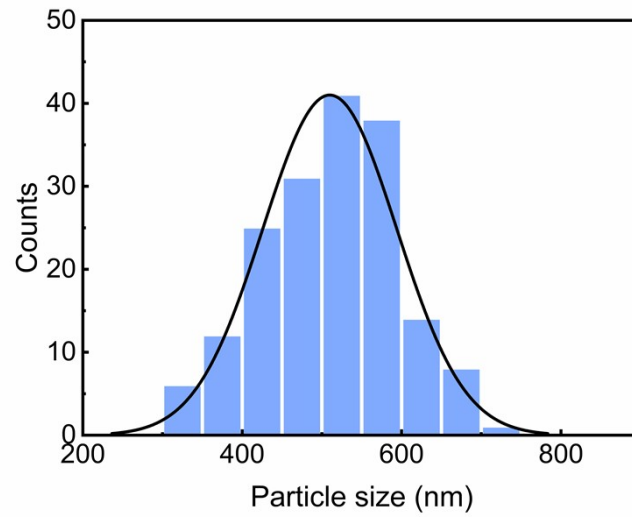
Figure S4. Particle size distribution diagram of IC@MnO$_2$. This statistic data shows an average size of about 500 nm. It should be noted that this IC@MnO$_2$ particle possesses a small building block as shown in Figure 3 in the main text.
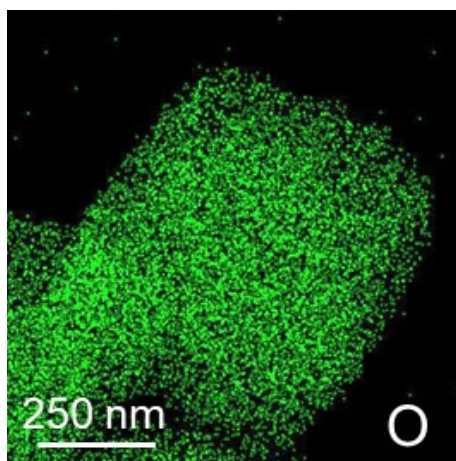
Figure S5. Energy dispersive X-ray spectroscopy (EDX) images of IC@MnO$_2$. This image shows the uniform distribution of O element.
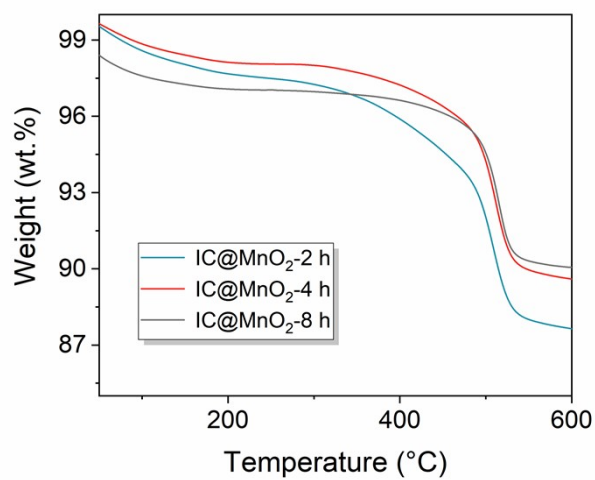
Figure S6. TG curve of IC@MnO$_2$ with different interstitial carbon content. The TG curves show that the interstitial carbon content of IC@MnO$_2$ is 4.93%, 3.91% and 3.22% at holding durations of 2, 4, and 8 h, respectively.
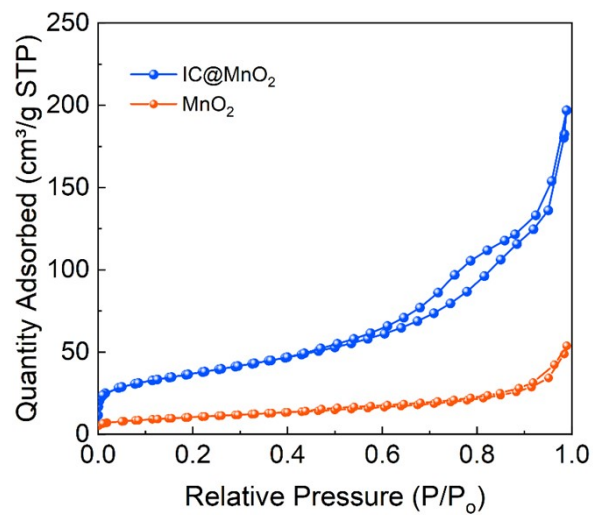
Figure S7. Nitrogen adsorption isotherms of IC@MnO$_2$ and MnO$_2$. It is apparent that IC@MnO$_2$ shows a mesoporous structure compared with MnO$_2$, which is beneficial to the ion transfer.
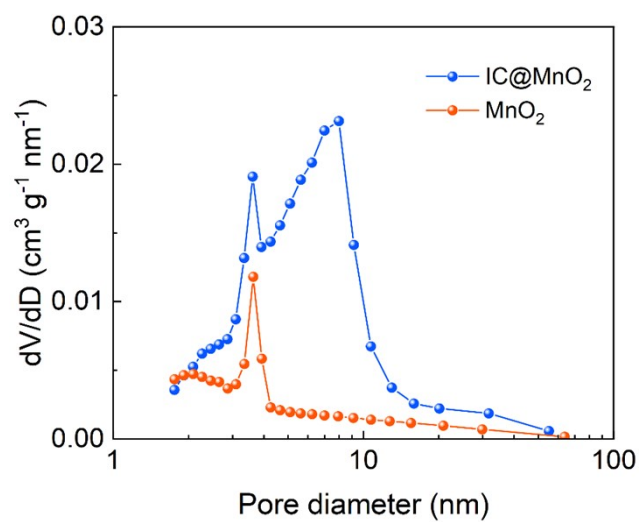
Figure S8. The pore size distribution of IC@MnO$_2$ and MnO$_2$. These data directly demonstrate the mesoporous structure of IC@MnO$_2$.
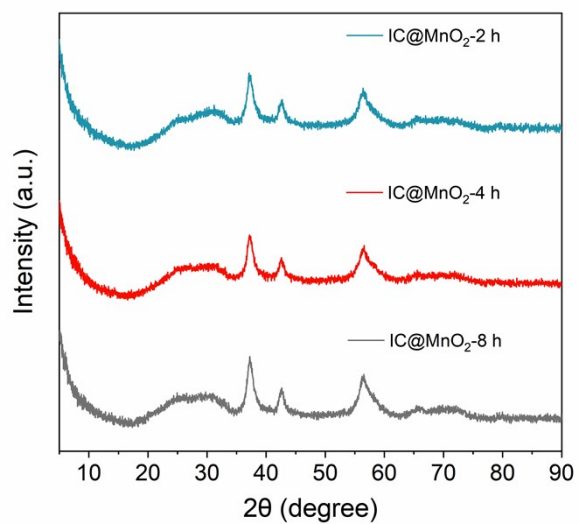
Figure S9. XRD pattern of IC@MnO$_2$ with different interstitial carbon content. This XRD data show that IC@MnO$_2$ with different interstitial carbon content exhibits similar characteristic peaks.
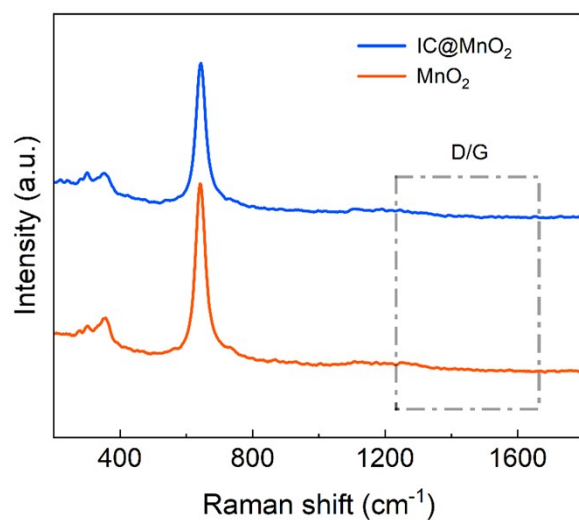
Figure S10. The Raman spectra of IC@MnO$_2$ and bare MnO$_2$ in the range of 200-1800 cm^{-1}. This Raman data implies that the carbon materials in IC@MnO$_2$ is such slight that the typical signals of D and G peaks were not detected, evidencing the existence form of interstitial carbon once again.
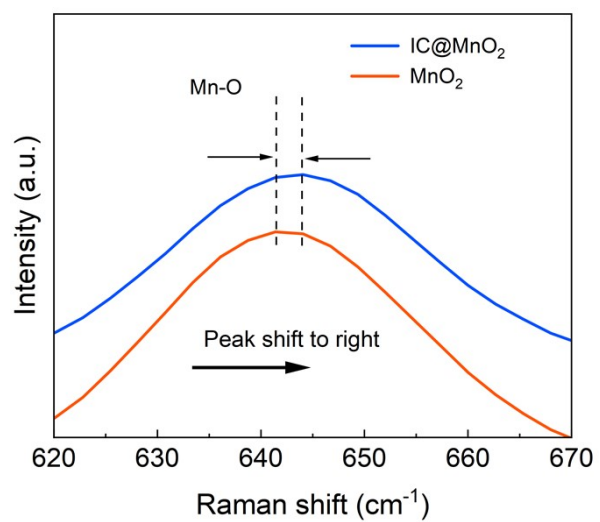
Figure S11. The Raman spectra of IC@MnO$_2$ and bare MnO$_2$ in the range of 600-800 cm^{-1}. We can find the peak shift of Mn-O due to the introduction of interstitial carbon.
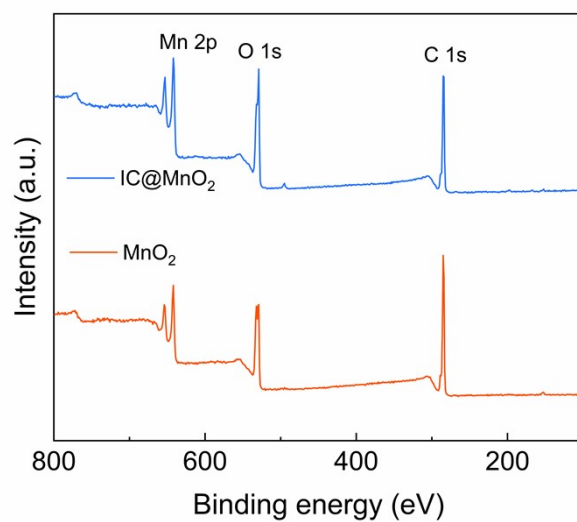
Figure S12. X-ray photoelectron spectroscopy (XPS) spectra for IC@MnO$_2$ and bare MnO$_2$. These XPS data detect the signals of Mn, O, and C.
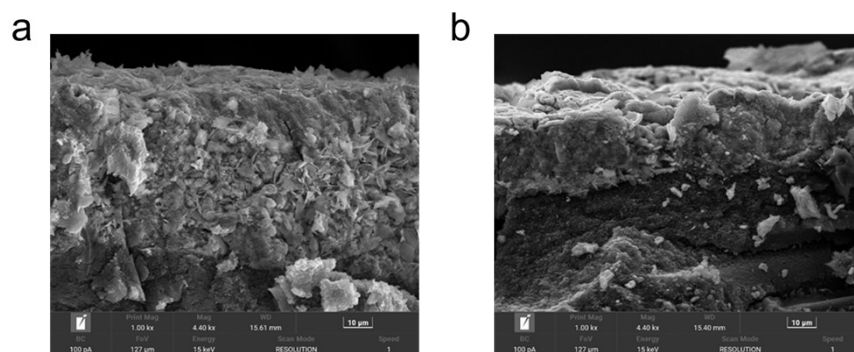
Figure S13. Cross-section SEM images of (a) IC@MnO$_2$ and (b) bare MnO$_2$ with a high loading mass.
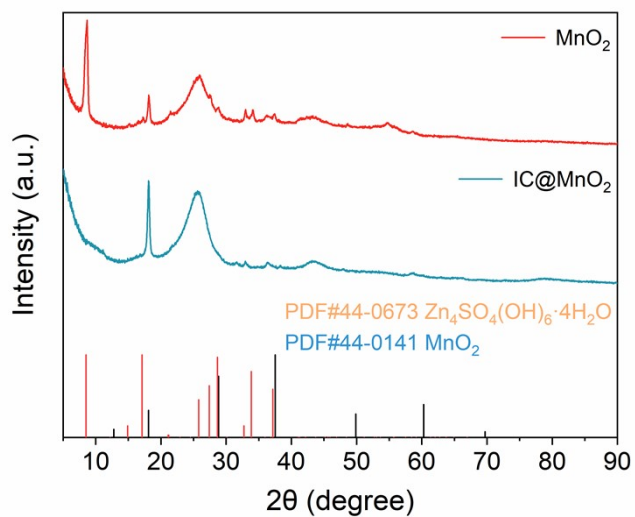
Figure S14. XRD pattern of MnO$_2$ and IC@MnO$_2$ electrodes after repeated charging/discharging cycles. Apparent peaks of alkaline zincate appeared appear for the MnO$_2$ electrode compared with the IC@MnO$_2$ electrode after cycling.
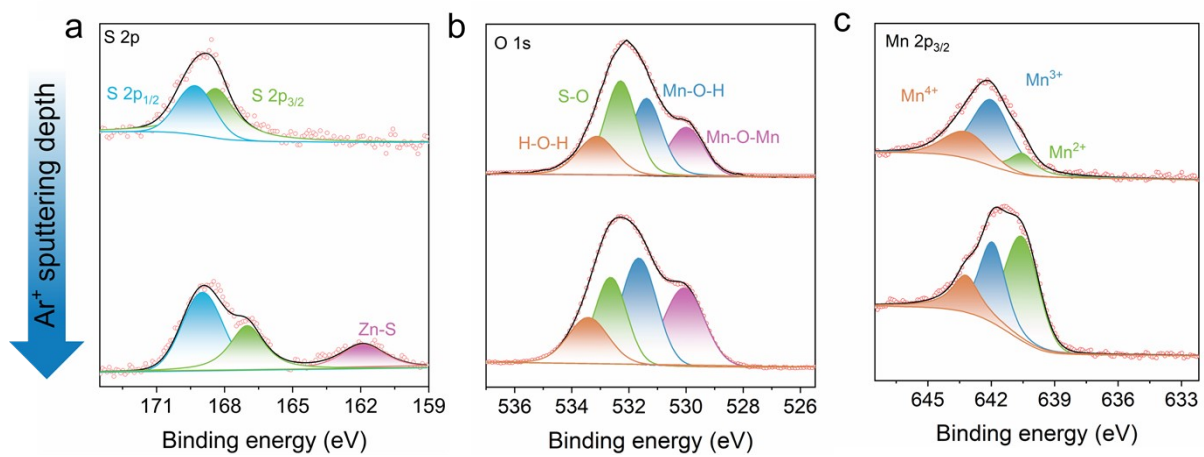
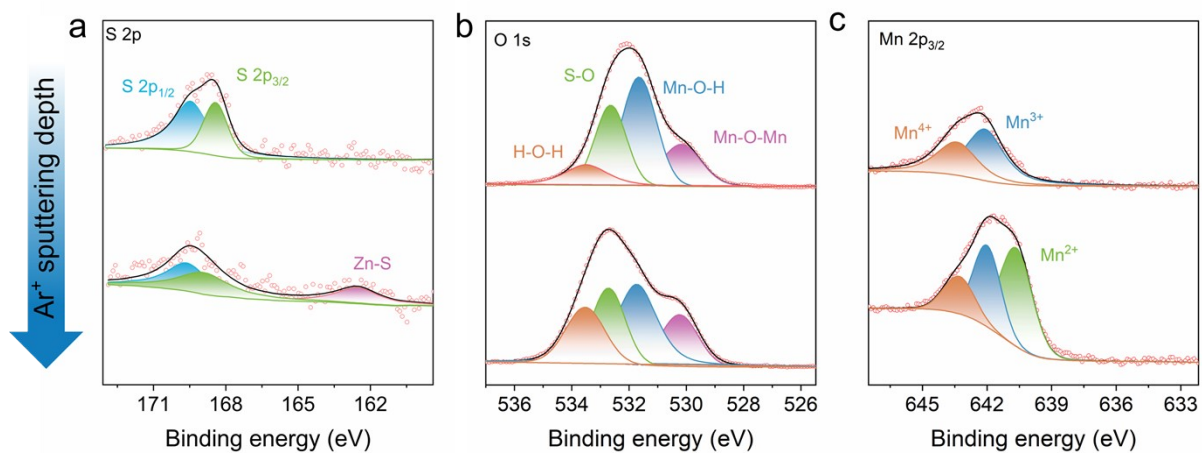**Figure S15.** Depth profiling XPS spectra of MnO_2: (a) S, (b) O, and (c) Mn.

Figure S16. Depth profiling XPS spectra of IC@MnO$_2$: (a) S, (b) O, and (c) Mn.
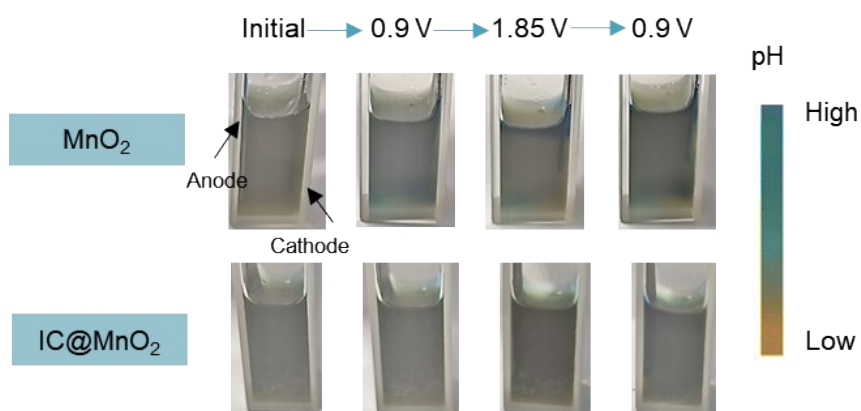
Figure S17. pH monitoring during the charging/discharging process. We add bromocresol green (dissolved in 1% (w/w) ethanol) in the electrolyte (2 M $ZnSO_4$ + 0.1 M $MnSO_4$) to monitor the pH change. The initial color of the electrolyte is grayish yellow, and the MnO_2 electrode interface changed to light blue after the charging and discharging process. In contrast, the $IC@MnO_2$ electrode interface maintains a stable pH throughout the charging/discharging process.
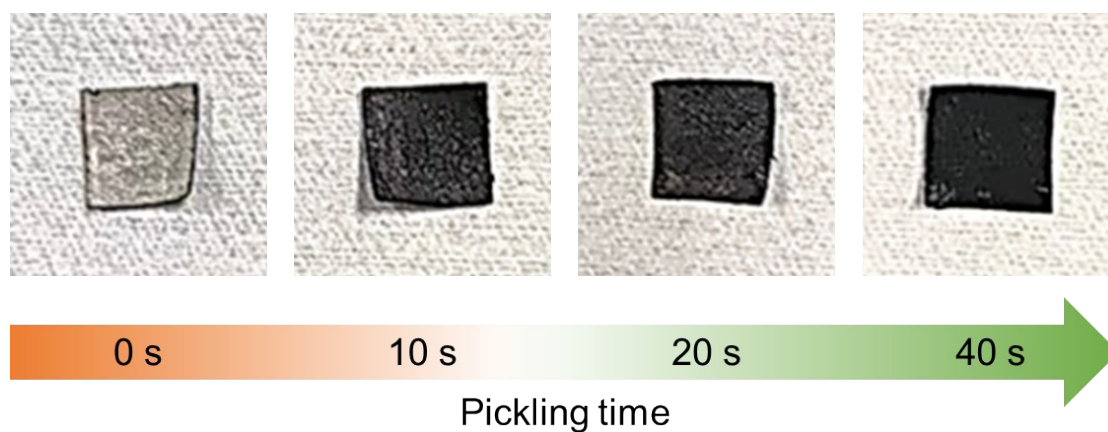
Figure S18. Digital images of the electrode surface under different pickling time. With increasing the pickling time from 0 to 40 s, we can see that the white surface rapidly changes to black due to the removal of alkaline zincate by acid.
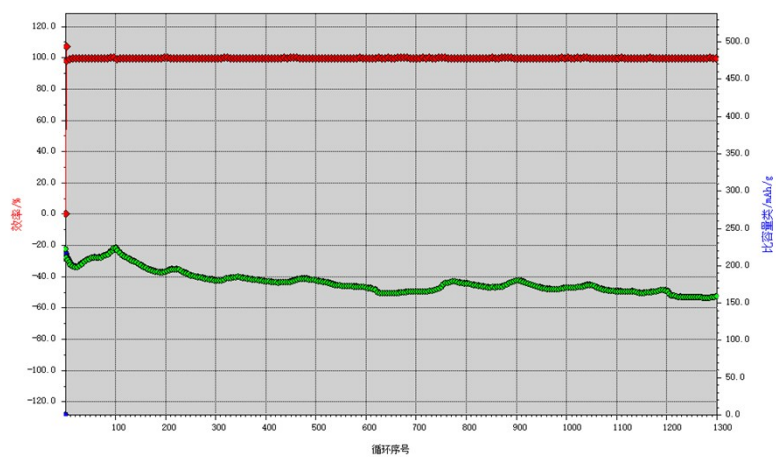
Figure S19. The corresponding source data of the long-term cycling performances of IC@MnO$_2$ at 2 A g^{-1}. We can see that specific capacity of charging/discharging processes maintains relatively stable during the 1300 cycles, while the capacity variation is due to the external environmental influences such as the temperature.
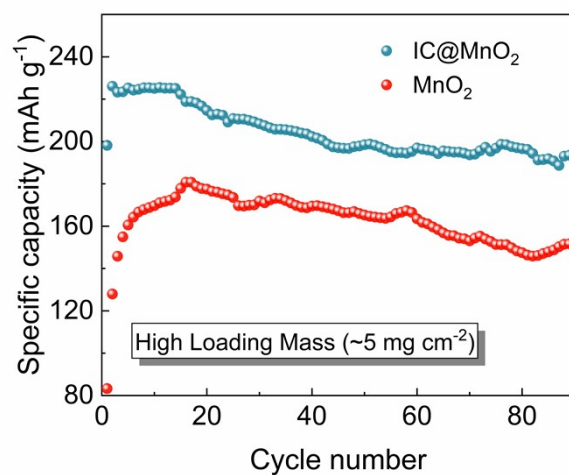
Figure S20. The cycling performance under a large loading mass (~5 mg cm^{-2}). We can see that IC@MnO$_2$ exhibits a higher specific capacity than the bare MnO$_2$ at the loading mass of ~5 mg cm^{-2}.
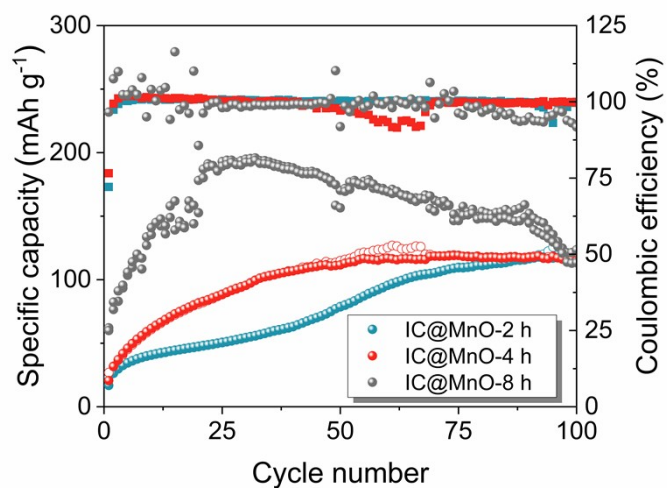
Figure S21. The cycling performance of IC@MnO$_2$ with different interstitial carbon content under a loading mass of ~5 mg cm^{-2}. We can see that IC@MnO$_2$-2 h and IC@MnO$_2$-4 h electrodes show a low specific capacity, and IC@MnO$_2$-8 h electrode exhibits poor stability although a relatively high specific capacity was achieved.
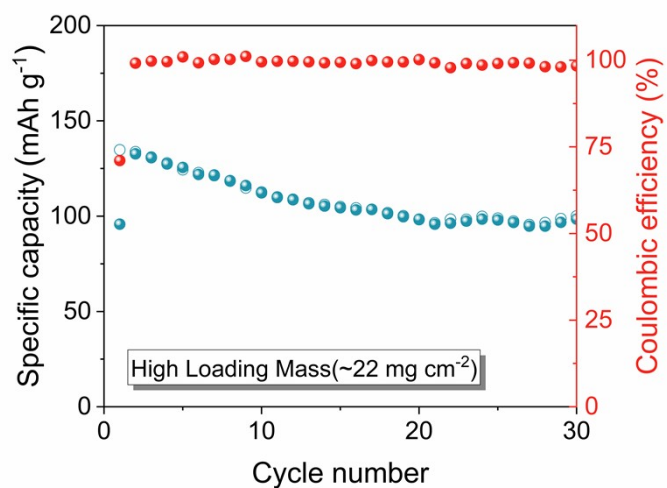
Figure S22. Coulombic efficiency and capacity of Zn∥IC@MnO$_2$ battery under a large loading mass of ~22 mg cm^{-2} at the current density of 0.05 A g^{-1}. We can see that IC@MnO$_2$ still release a high specific capacity during the electrode scaleup process.
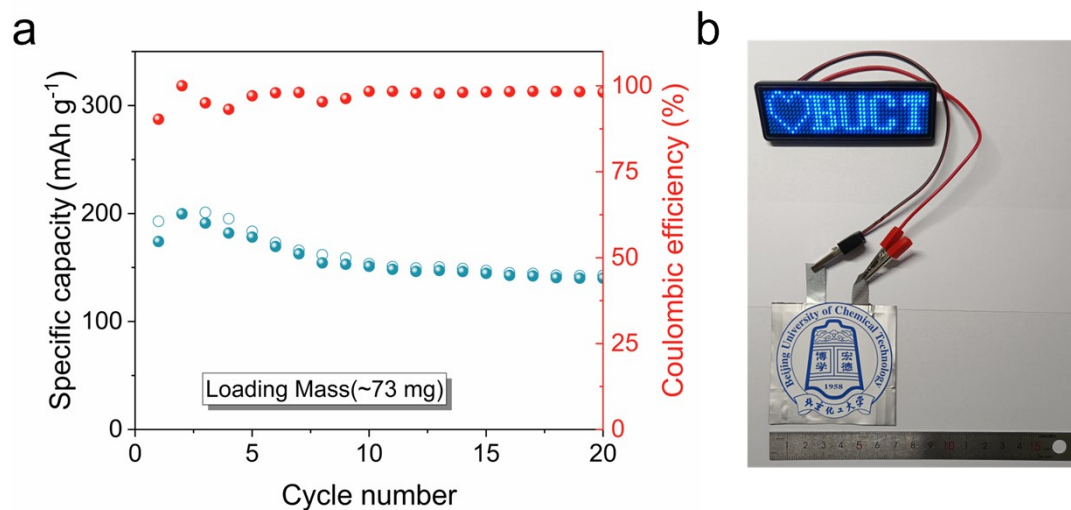
Figure S23. (a) Coulombic efficiency and capacity of Zn‖IC@MnO$_2$ pouch cell (4×4 cm^2) at the current density of 0.05 A g^{-1}. (b) Digital photos of a blue LED device powered by the Zn‖IC@MnO$_2$ pouch cell.

Table S1 The maximum peak ratio of Mn^{4+}/Mn^{3+} for Mn $2p_{1/2}$ and Mn $2p_{3/2}$, respectively.

Sample	Valence state	Mn $2p_{3/2}$	
		Maximum peak	Mn^{4+}/Mn^{3+}
IC@MnO$_2$	Mn^{3+}	26354	0.211
	Mn^{4+}	5573	
MnO$_2$	Mn^{3+}	18089	0.271
	Mn^{4+}	4906	

Table S2. Summary of the electrochemical performance of Mn-based cathode materials in ZIBs.

Cathode	Specific capacity/Rate performance	Cycling performance	Reference
β-MnO$_2$ [1]	225 mAh g^{-1} at 0.65 C	94% capacity retention over 2000 cycles at 6.5 C	Nat. Commun. 2017, 8, 405.
Co-Mn$_3$O$_4$ [2]	220 mAh g^{-1} at 0.1 mA g^{-1}	71% capacity retention over 4 A g^{-1} over 1000 cycles	Adv. Energy Mater. 2020, 2003203.
K$_{0.27}$MnO$_2$·0.54H$_2$O [3]	280 mAh g^{-1} at 0.1 mA g^{-1}	86% capacity retention over 100 cycles at 0.1 A g^{-1}	Adv. Energy Mater. 2021, 2101287
α-MnO$_2$/C [4]	272 mAh g^{-1} at 66 mA g^{-1}	69% capacity retention over 50 cycles at 66 mA g^{-1}	J. Energy Chem. 2017, 26, 815-819.
S-MnO$_2$ [5]	324 mAh g^{-1} at 0.2 A g^{-1}	95% capacity retention over 100 cycles at 2 A g^{-1}	Energy Storage Mater. 2022, 47, 424-433.
Bi-MnO$_2$ [6]	365 mAh g^{-1} at 0.1 A g^{-1}	93% capacity retention over 10000 cycles at 1 A g^{-1}	Energy Storage Mater. 2022, 48, 212-222.
Mo-MnO$_2$ [7]	459.7 mAh g^{-1} at 0.2 A g^{-1}	-	Nano Res. 2022, 16, 2511-2518.
N-MnO$_2$ [8]	360 mAh g^{-1} at 0.1 A g^{-1}	80.4% capacity retention over 1000 cycles at 1 A g^{-1}	J. Phys. Chem. C 2021, 125, 20195-20203.
Fe-MnO$_2$ [9]	338.2 mAh g^{-1} at 1 A g^{-1}	86.3% capacity retention over 200 cycles at 1 A g^{-1}	J. Power Sources 2022, 527.
IC@MnO$_2$	335.5 mAh g^{-1} at 0.2 A g^{-1}	80.25% capacity retention over 1300 cycles at 2 A g^{-1}	*This work*

References

1. N. Zhang, F. Y. Cheng, J. X. Liu, L. B. Wang, X. H. Long, X. S. Liu, F. J. Li and J. Chen, *Nat. Commun.*, 2017, **8**, 405.

2. J. Ji, H. Wan, B. Zhang, C. Wang, Y. Gan, Q. Tan, N. Wang, J. Yao, Z. Zheng, P. Liang, J. Zhang, H. Wang, L. Tao, Y. Wang, D. Chao and H. Wang, *Adv. Energy Mater.*, 2020, **11**, 2003203.

3. L. Liu, Y. C. Wu, L. Huang, K. Liu, B. Duployer, P. Rozier, P. L. Taberna and P. Simon, *Adv. Energy Mater.*, 2021, **11**, 2101287.

4. S. Islam, M. H. Alfaruqi, J. Song, S. Kim, D. T. Pham, J. Jo, S. Kim, V. Mathew, J. P. Baboo, Z. Xiu and J. Kim, *J. Energy Chem.*, 2017, **26**, 815-819.

5. Y. Zhao, P. Zhang, J. Liang, X. Xia, L. Ren, L. Song, W. Liu and X. Sun, *Energy Storage Mater.*, 2022, **47**, 424-433.

6. Y. Ma, M. Xu, R. Liu, H. Xiao, Y. Liu, X. Wang, Y. Huang and G. Yuan, *Energy Storage Mater.*, 2022, **48**, 212-222.

7. X. Xia, Y. Zhao, Y. Zhao, M. Xu, W. Liu and X. Sun, *Nano Res.*, 2022, **16**, 2511-2518.

8. Z. Zhang, S. Li, B. Zhao, X. Zhang, X. Wang, Z. Wen, S. Ji and J. Sun, *J. Phys. Chem. C*, 2021, **125**, 20195-20203.

9. H. Li, Z. Huang, B. Chen, Y. Jiang, C. Li, W. Xiao and X. Yan, *J. Power Sources*, 2022, **527**, 231198.